Journal of Multidisciplinary Modeling and Optimization

Volume:4

Issue:1

Editor in Chief

Ahmet ŞAHİNER

E-ISSN: 2645-923X

http://dergipark.gov.tr/jmmo

Editor in Chief

Editorial Board

TABLE OF CONTENTS

Model for Retail Price Forecast of Thailand Rice In Plateau State Nigeria

O. ADEDIRE*[1], A. J. ANGYAK[2], O. O. ADEDIRE[3], and K. COLLINA[4]

[1]Department of Mathematics,
University of Jos, Jos, Plateau State, Nigeria
dharenss@gmail.com
ORCID: https://orcid.org/0000-0003-3790-7776

[1]Federal College of Forestry, Jos, Plateau State, Nigeria,
dharenss@gmail.com

[2]Department of Actuarial Science,
University of Jos, Jos, Plateau State, Nigeria
angyakjonathan@gmail.com
ORCID: https://orcid.org/0000-0002-6117-1458

[3]Federal College of Forestry Mechanization, Afaka, Kaduna, Kaduna State, Nigeria,
defemzz@yahoo.com
ORCID: https://orcid.org/0000-0003-3010-2043

[4]Federal College of Forestry, Jos, Plateau State, Nigeria,
Talk2nev@yahoo.com
ORCID: https://orcid.org/0000-0002-3296-4643

Received: 30.01.2021, Accepted: 23.04.2021, Published: 03.01.2022

Abstract — *In this paper, monthly retail prices of imported Thailand rice in Plateau State are analyzed and a model is proposed. Data were collected from major warehouses of businessmen in Plateau State capital and based on the observed pattern in the raw data, time series analysis was employed. Particularly, Seasonal Autoregressive Integrated Moving Average (SARIMA) method is used on the data which covered a period of 156 months (January 2007- December 2019). Results from SARIMA (1, 1, 0)(0,1,1) show Ljung –Box Q statistics value of 30.843 with p value of 0.104 and R-squared value of 0.997 at 95% confidence bound which are all indicative of adequate fitted model for forecast. Hence the developed model from SARIMA (1, 1, 0)(0,1,1) can be used to predict monthly retail prices of Thailand rice in Plateau State Nigeria to aid government policy and enable adequate planning for future changes in retail price of rice.*

Keywords: Model, Rice Retail, Price, Forecast.
Mathematics Subject Classification: 91B26, 91B60, 91B60, 00A71, 03C30.

Cite as: *O. Adedire, A. J. Angyak, O.O. Adedire and C. Kambai, Model for retail price forecast of Thailand rice in Plateau State, Nigeria, Journal of Multidisciplinary Modeling and Optimization 4(1) (2021), 1-10.*

1 Introduction

Rice (Oryza sativa) is a cash crop which is commonly found as a staple food in many households in Plateau State Nigeria. Studies have shown that many rice consumers in Nigeria eat more foreign rice than the domestic rice [1]. One of the reasons being that farmers who are mainly involved in domestic rice production could not meet up with consumption rate due to small-scale farming, terrorist attacks, farmer-herder clashes, consequently increase in prices of foreign food commodity is inevitable [2]. Another reason despite government intervention is presence of small stone particles in some of the domestic rice available due to crude method of processing as only a few number of standard rice processing plants are fully functional. Rice - among other staple foods - take about 6 percent of household expenses in Nigeria [3].
Over the years, people of Plateau State have depended heavily on foreign rice imported from different countries of the world. There are different varieties of rice in Nigeria but rice imported from Thailand is one of the highly desired varieties by the residents of Plateau State. While there are different reasons for consumers' preferences for certain varieties of rice [4], preference of Plateau State residents for Thailand rice could be due to increasing awareness of consumers about quality of rice in West African countries [5].

Many Plateau State residents prefer buying their rice from open markets and from small retail shop outlets than from supermarkets and other formal superstores mainly due to lower prices of the food commodity which supports the findings of Basorun [6].
While some studies exist on heavy and trace elements in some brands of rice consumed outside of Plateau State in Nigeria [7], other studies consider trend, regulation, processing and safety of food [8, 9, 10, 11, 12, 13]. The choice of SARIMA is due to its ability to predict accurately with few numbers of available parameters [14]. It uses lag and shift of historical seasonal data to forecast future outline.
From the foregoing and researches in literature, there has not been a research to model retail price of Thailand rice in Plateau State Nigeria. In this study, our aim is to create a model for retail price forecast of Thailand rice in Plateau State Nigeria to aid government policy and enable adequate planning for future changes in price. The remaining part of this paper is arranged as follows: section 2 centres on the materials and methods which include the study area, data analysis and model specification. In sections 3 and 4, results and discussion are presented and finally conclusion comes up in section 5.

2 Materials and Methods

2.1 Study Area

The study area for this research is Yan Kwalli market situated in the area of Terminus market in Jos North Local Government Area of Plateau State, Nigeria. It is one of the major markets in Plateau State where all kinds of foreign rice brands are sold. Data for this study were collected from different warehouses and retail prices of Thailand rice were extracted from the records of businessmen in the market (2007-2019). Some of the dealers in the sales of foreign rice did not keep records of their past sales. It should be noted that average retail prices of daily and monthly data are used for this study due to variations in retail prices of foreign rice.

2.2 Data Analysis

The data for this study is analyzed using Seasonal Auto-Regression Integrated Moving Average (SARIMA) method of Time Series analysis with aid of Statistical Package for Social Sciences (SPSS). The MAPLE software package is also employed to simplify the series equation.

2.3 Specification of the Model

The model for this study is multiplicative seasonal model defined by

$$SARIMA(p,d,q)(P,D,Q)_s \tag{1}$$

where p and P are the number of auto-regressive component of retail price of Thailand rice for both non seasonal and seasonal components respectively. While the parameters d and D are the number of times of differencing the retail prices of Thailand rice for non seasonal and seasonal components respectively, q and Q represent the number of moving average components of the retail price of Thailand rice for non seasonal and seasonal components with s representing the length of the seasonal period. Hence the generalized form of (1) for a series Y_t is given as [15, 16]:

$$\emptyset_p(B)\Phi_P(B^s)\Delta\,\Delta^* Y_t = \theta_q(B)\Theta_Q(B^s)\,\varepsilon_t \tag{2}$$

where ε_t is white noise, residual or disturbance, B is a backshift operator, $\Delta = (1-B)^d$ and $\Delta^* = (1-B)^d$ are nonseasonal and seasonal differencing operators and

$$\emptyset_p(B) = 1 - \emptyset_1 B - \emptyset_2 B^2 - \cdots - \emptyset_p B^p \tag{3}$$
$$\Phi_P(B^s) = 1 - \Phi_1 B^s - \Phi_2 B^{2s} - \cdots - \Phi_P B^P \tag{4}$$
$$\theta_q(B) = 1 - \theta_1 B - \theta_2 B^2 - \cdots - \theta_q B^q \tag{5}$$
$$\Theta_Q(B^s) = 1 - \Theta_1 B^s - \Theta_2 B^{2s} - \cdots - \Theta_Q B^Q \tag{6}$$

3 Results

The results from the analysis of the retail price of Thailand rice in Plateau State covering a period of 156 months from January 2007 to December 2019 are shown in tables and figures below:

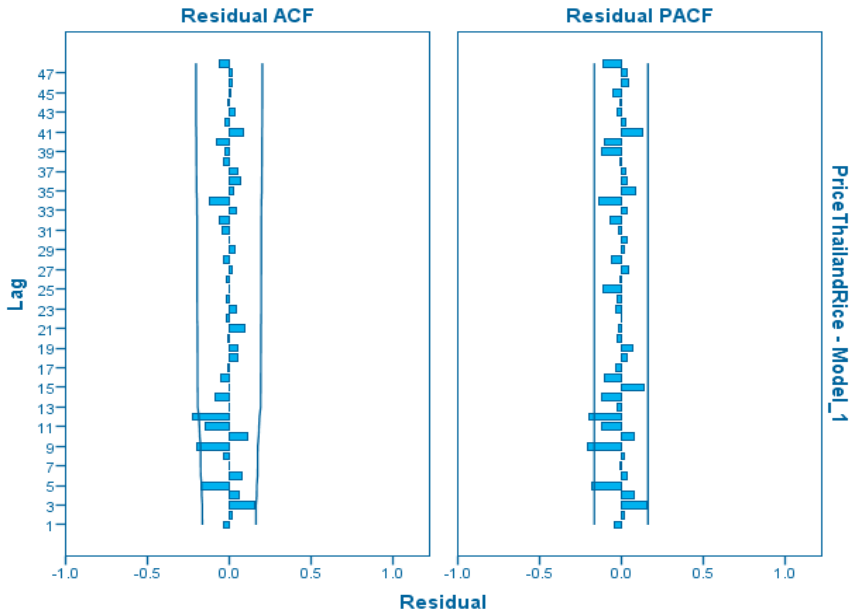

Figure 1: Residual Auto-correlation Function (ACF) and Partial ACF for retail price of Thailand rice (2007-2019) for SARIMA (1, 1, 0) (0, 1, 1) at 48 lags.

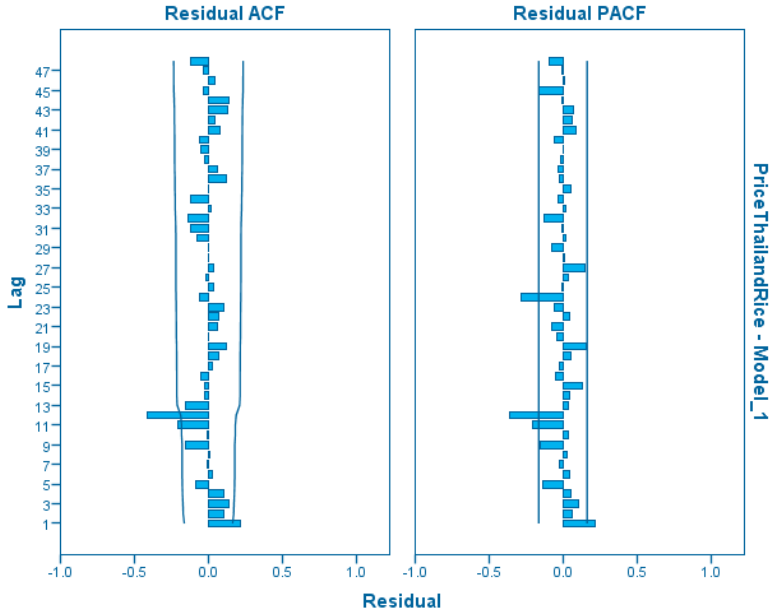

Figure 2: Residual Auto-correlation Function (ACF) and Partial ACF for retail price of Thailand rice (2007-2019) for SARIMA (1, 0, 0) (0, 1, 0) at 48 lags.

Table 1: Fit Statistics of the SARIMA (1, 1, 0) (0, 1, 1) Model of Time Series Analysis.

Model	Stationary R-squared	R Squared	Root Mean Square Error	Normalized BIC
Retail price of Thai-land rice (N)	0.736	0.997	295.205	11.688

a. Best-Fitting model according to R-Squared.

Table 2: Fit Statistics of the SARIMA (1, 0, 0) (0, 1, 0) Model of Time Series Analysis.

Model	Stationary R-squared	R Squared	Root Mean Square Error	Normalized BIC
Retail price of Thai-land rice (N)	0.965	0.995	404.153	12.314

b. Best-Fitting model according to R-Squared.

Table 3: Ljung-Box parameters of the SARIMA (1, 1, 0) (0, 1, 1) Model of Time Series Analysis.

Model	Ljung-Box statistics	df	Sig.
Retail price of Thailand rice (N)	30.843	16	0.104

Table 4: Ljung-Box parameters of the SARIMA (1, 0, 0) (0, 1, 0) Model of Time Series Analysis.

Model	Ljung-Box statistics	df	Sig.
Retail price of Thailand rice (N)	57.165	17	0.00

Table 5: Coefficients of SARIMA (1, 1, 0) (0, 1, 1) model for the governing equation for the retail price (in Nigerian Naira N) of Thailand rice.

SARIMA(1, 1, 0)(0, 1, 1)	Coefficients	SE	t	Sig.
AR lag 1	0.167	0.081	2.055	0.042
Seasonal MA lag 1	0.918	0.126	7.281	0.000

Table 6: Comparison of average original retail price (in Nigerian Naira N) with model "fit" price within the period of coverage for the last two consecutive years.

	Original Retail Price		SARIMA(1,1,0)(0,1,1) Model Fit Price	
Month	2018	2019	2018	2019
Jan	18650.00	23000.00	18647.93	23181.17
Feb	18920.00	22500.00	18542.62	22924.81
Mar	19610.00	23300.00	19466.99	22933.93
Apr	19700.00	23600.00	19873.80	23563.54
May	20590.00	23550.00	19779.84	23801.54
Jun	20680.00	23550.00	20919.74	23697.40
Jul	20685.00	23200.00	20950.38	23776.98
Aug	21650.00	23320.00	21445.67	23261.17
Sep	21690.00	23700.00	21611.32	23921.45
Oct	21980.00	24400.00	22223.95	24154.14
Nov	22200.00	24600.00	22388.91	24857.05
Dec	23100.00	24800.00	22632.01	25078.81

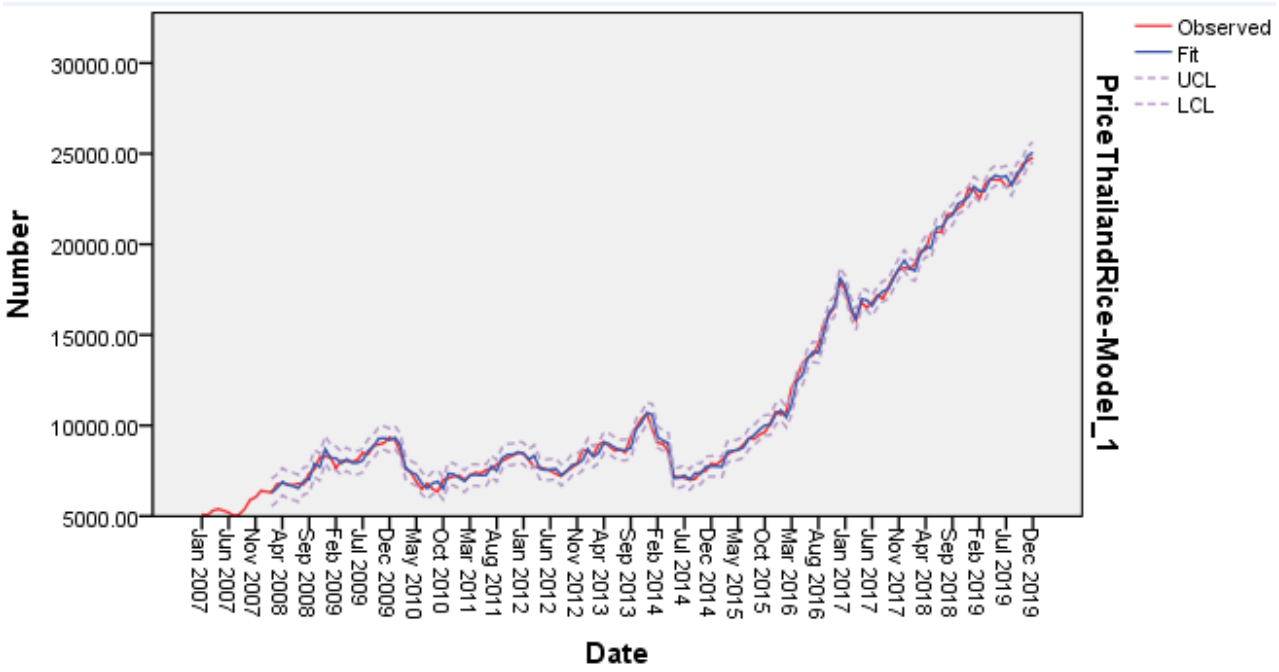

Figure 3: Seasonal ARIMA (1, 1, 0) (0, 1, 1) model chart of the retail price of Thailand rice (2007-2019).

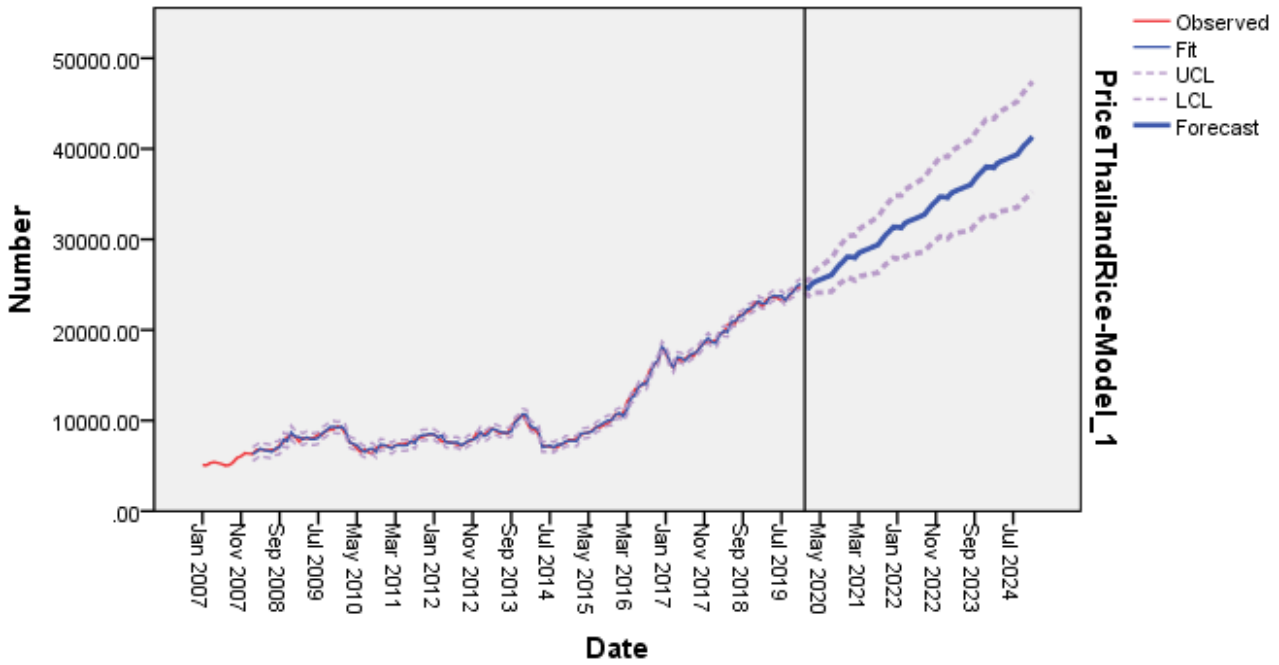

Figure 4: Seasonal ARIMA (1, 1, 0) (0, 1, 1) model chart of the retail price of Thailand rice (2007-2019) with forecast (2020-2024) Plateau State.

Table 7: Forecast (2020 - 2024) of retail price (in Nigerian Naira N) of Thailand Rice using the governing equation (15) for SARIMA (1, 1, 0) (0, 1, 1) .

Month	Year				
	2020	2021	2022	2023	2024
Jan					
Feb	24745.43	28052.98	31369.99	34687.00	38004.01
Mar	24634.23	27949.67	31266.67	34583.68	37900.69
Apr	25170.52	28487.26	31804.27	35121.28	38438.29
May	25393.84	28710.80	32027.81	35344.82	38661.83
Jun	25556.80	28873.80	32190.81	35507.82	38824.82
Jul	25724.58	29041.59	32358.60	35675.60	38992.61
Aug	25920.36	29237.37	32554.38	35871.38	39188.39
Sep	26078.54	29395.55	32712.56	36029.56	39346.57
Oct	26663.65	29980.66	33297.66	36614.67	39931.68
Nov	27177.19	30494.20	33811.21	37128.22	40445.23
Dec	27576.80	30893.81	34210.82	37527.83	40844.84
	28060.30	31377.31	34694.31	38011.32	41328.33

4 Discussion

Two SARIMA methods of time series analysis are considered. They include SARIMA (1, 1, 0) (0, 1, 1) and SARIMA (1, 0, 0) (0, 1, 0). From the preliminary investigation of the raw data, measure of central tendency show a shift in the mean over time in upward manner. In order to make the non stationary mean steady, differencing of the retail price of Thailand rice was done to remove both the local trend component and seasonal trend component. The model considered that each retail price depends on one previous retail price for nonseasonal component and one random shock for seasonal component. Hence equation (1) for parameters p = 1, d = 1, q = 0, P = 0, D = 1, Q = 1 becomes SARIMA (1, 1, 0) (0, 1, 1) at 95% confidence bounds. The residual Auto-Correlation Functions (ACF) and residual Partial Autocorrelation Function (PACF) for SARIMA (1, 1, 0) (0, 1, 1) at 95% confidence bounds are shown in Figure 1. However, for the alternative SARIMA method of time series analysis, the non stationary mean was made steady by differencing of the retail price of Thailand rice to remove seasonal trend component only without random shock for seasonal component and with consideration of the dependence of each retail price on one previous retail price for nonseasonal component. Hence equation (1) for parameters p = 1, d = 0, q = 0, P = 0, D = 1, Q = 0 becomes SARIMA (1, 0, 0) (0, 1, 0) at 95% confidence bounds. The residual Auto-Correlation Functions (ACF) and residual Partial Autocorrelation Function (PACF) for SARIMA (1, 0, 0) (0, 1, 0) at 95% confidence bounds are shown in Figure 2.

From Tables 1 and 2, the R-squared values are 0.997 and 0.995 for SARIMA (1, 1, 0) (0, 1, 1) and SARIMA (1, 0, 0) (0, 1, 0) respectively which indicate good fitted models such that the models predict the observed values well. Table 3 shows the Ljung-Box Q values of 30.843 with significance $p^* = 0.104$ which indicate that error not explained is merely a random error and that the residuals of the model does not have significant autocorrelation left as shown in Figure 1. Hence we fail to reject null hypothesis which states that there is no significant auto correlation left in the residual of the associated model. On the other

hand, Table 4 shows the Ljung-Box Q values of 57.165 with significance $p^* = 0.00$ which indicate that error not explained is a significant random error and that the residuals of the model have significant autocorrelation left as shown in Figure 2. Hence we fail to reject alternate hypothesis which states that there is significant auto correlation left in the residual of the associated model. Furthermore, SARIMA (1, 1, 0) (0, 1, 1) has lower Root Mean Square Error (295.205) compared to SARIMA (1, 0, 0) (0, 1, 0) with RMSE (404.153) as indicated in Tables 1 and 2 respectively. From the foregoing, the SARIMA (1, 1, 0) (0, 1, 1) model is preferable to SARIMA (1, 0, 0) (0, 1, 0) model, hence the focus is shifted to SARIMA (1, 1, 0) (0, 1, 1) in the rest of this analysis.
From Table 5, the results show coefficients of SARIMA (1, 1, 0) (0, 1, 1) model for the governing equation of Thailand rice which indicate that the coefficients are statistically significant and should be retained in the model series equation. Using Table 5 with SARIMA $(1, 1, 0) (0, 1, 1)_s$, the equations (2)-(6) give the following:

$$\emptyset_1(B)\Phi_0(B^s)\Delta\,\Delta^* Y_t = \theta_0(B)\Theta_1(B^s)\,\varepsilon_t \tag{7}$$
$$\emptyset_1(B)\Phi_0(B^s)(1-B)^1(1-B^s)^1 Y_t = \theta_0(B)\Theta_1(B^s)\,\varepsilon_t \tag{8}$$

From equations (4) and (5), $\Phi_0(B^s) = 1$ and $\theta_0(B) = 1$ hence (8) gives

$$\emptyset_1(B)(1-B)^1(1-B^s)^1 Y_t = \Theta_1(B^s)\,\varepsilon_t \tag{9}$$

Application of (3) and (6) on (9) with the aid of Maple software give

$$(1-\emptyset_1 B^1)(1-B)(1-B^s)^1 Y_t = (1+\Theta_1 B^s)\,\varepsilon_t \tag{10}$$

which on expansion becomes

$$[(1-\emptyset_1 B)(1-B^s-B+BB^s)]Y_t = (1+\Theta_1 B^s)\,\varepsilon_t \tag{11}$$
$$[1-B^s-B+BB^s-\emptyset_1 B+\emptyset_1 BB^s+\emptyset_1 BB-\emptyset_1 BBB^s)]Y_t = (1+\Theta_1 B^s)\,\varepsilon_t \tag{12}$$

Expansion of (12) gives

$$Y_t - Y_{t-s} - Y_{t-1} + Y_{t-s+1} - \emptyset_1 Y_{t-1} + \emptyset_1 Y_{t-s+1} + \emptyset_1 Y_{t-2} - \emptyset_1 Y_{t-s+2} = \varepsilon_t + \Theta_1 \varepsilon_{t-s} \tag{13}$$

From Table 5, $\emptyset_1 = 0.167$ and $\Theta_1 = 0.918$

$$Y_t - Y_{t-s} - Y_{t-1} + Y_{t-s+1} - 0.167\,Y_{t-1} + 0.167\,Y_{t-s+1} + 0.167\,Y_{t-2} - 0.167\,Y_{t-s+2} = \varepsilon_t + 0.918\,\varepsilon_{t-s} \tag{14}$$

With the length of the seasonal period $s = 12$ and on further simplification, Eq. (14) gives

$$Y_t = 1.167\,Y_{t-1} - 0.167\,Y_{t-2} + Y_{t-12} - 1.167\,Y_{t-13} + 0.167\,Y_{t-14} + \varepsilon_t + 0.918\,\varepsilon_{t-12} \tag{15}$$

where Y_t is the retail price of Thailand rice at the current time and Y_{t-i} $(i = 1, 2, \ldots)$ are values of previous retail prices at previous monthly times. The ε_t and ε_{t-i} represent random shocks at current times and previous times respectively. Hence equation (15) is the model equation representing the evolution of retail price of Thailand rice in Plateau State. Figure 3 shows the comparison of the fitted model of retail prices of Thailand rice in Plateau State with the actual raw data. Moreover, values for two consecutive years 2018 and 2019 only are displayed in Table 6 to show similarity of fitted model with the actual raw data. It can be seen that the fitted model closely look like the raw data over the number of years covered from January (2007) to December (2019), this is an indication of appropriateness of the model to explain the changes in time series analysis of the retail price of the Thailand rice in Plateau State Nigeria. In Figure 4 and Table 7, five-year forecast of the retail price of the Thailand rice in Plateau State is predicted. A rise in trend of the retail prices is observed over the period of forecast January (2020) - December (2024).

5 Conclusion

A SARIMA model was developed to examine the trend in retail prices of Thailand rice in Plateau State, Nigeria. Data which covered a period of 156 months were collected from warehouses of major rice dealers in Yan kwalli market - one of the main markets specialized in sales of domestic and foreign rice - in Terminus area of Jos, the Plateau state capital. After the analysis using SARIMA (1, 1, 0) (0, 1, 1), we derived a model equation which is capable of predicting future changes in retail prices of Thailand rice in Plateau State, Nigeria when existing factors have not significantly changed.

Conflict of Interest Declaration

The authors declare that there is no conflict of interest statement.

Ethics Committee Approval and Informed Consent

The authors declare that there is no ethics committee approval and/or informed consent statement.

References

[1] K. Gyimah-Brempong, M. Johnson and H. Takeshima, The Nigerian rice economy: Policy options for transforming production, marketing and trade, International Food Policy Research Institute (IFPRI), Washington DC, 2016.

[2] H. Takeshima and O. Bakare, Production systems: biophysical and economic environment and constraints. In: Gyimah - Brempong, K., Johnson,M., Takeshima, H. (Eds.), The Nigerian Rice Economy; Policy Options for Transforming Production, Marketing and Trade. University of Pennsylvania Press, Philadelphia, Pennsylvania, 2016.

[3] M. Johnson, H. Takeshima, K. Gyimah-Brempong, O. Kuku-Shittu, X. Diao, P. Dorosh, M. Malek, J. Koo, A. Pradesha and A. Ajibola, Policy options for accelerated growth and competi-

tiveness of the domestic rice economy in Nigeria. International Food Policy Research Institute, Washington DC, 2013.

[4] K. Aoki, K. Akai and K. Ujiie, A choice experiment to compare preferences for rice in Thailand and Japan: the impact of origin, sustainability and taste, Food Qual. Prefer., 56 2017, 274–284.

[5] M. Demont, and M. Ndour, Upgrading rice value chains: experimental evidence from 11 African Markets, Glob. Food Secur., 5 2015, 70–76.

[6] J. Basorun, Empirical analysis of association of rice marketing factors in Igbemo region, Nigeria, Int. J. Bus. Soc. Sci., 3(2) 2012, 296–306.

[7] K. Emumejaye, Heavy and trace elements in some brands of rice consumed in Delta State, Nigeria, IOSRJ. Appl. Phys., 6(2) 2014, 1–5.

[8] J. Ezirigwe, Much Ado about food safety regulation in Nigeria, J. Sustain. Develop. Law Policy, 9(1) 2018, 109–132.

[9] H.H. Jensen and J. Zhou, Food safety regulation and private standards in China. In: Hammoudi, A., Grazia,C., Surry,Y., Traversac,J.B. (Eds.), FoodSafety, Market Organization, Trade and Development. Springer, Cham, 2015.

[10] M. Johnson and A. Ajibola, Post-harvest processing, marketing and competitiveness of domestic rice. In: Gyimah-Brempong, K., Johnson, M.,Takeshima,H.,Gyimah-Brempong, K., Johnson, M., Takeshima, H. (Eds.), The Nigerian rice economy : Policy options for transforming production, marketing and trade. University of Pennsylvania Press, Philadelphia, 2016.

[11] M. Nguyen, M. Demont, E. Vanloo, A. deGuia, P. Rutsaert, T. Huutuan and W. Verbeke, What is the value of sustainably-produced rice? Consumer evidence from experimental auctions in Vietnam. Food Policy, 79, 2018, 283–296.

[12] R. Oginyi, O. Mbam, C. Abojei and O. James, Assessment of occupational health hazard and the use of safety measures among rice mill workers in Ebonyi state, Nigeria, World Appl . Sci. J., 35 (7) 2017, 1133–1141.

[13] D. Ray, N. Mueller, P. West and J. Foley, Yield trends are insufficient to double global crop production by 2050. PLoSOne 8(6) 2013, e66428.

[14] M.O. Thomas, Short Term Forecasting, an introduction the Box Jenkins Approach, John Wiley and Sons, 1983.

[15] G. E. P. Box, G. M. Jenkins and G. C Reinsel, Time Series Analysis: Forecasting and Control. John Wiley & Sons Inc., San Francisco, 2013.

[16] J. D. Cryer and K. –S. Chan, Time Series Analysis: with Applications in R. Springer, New York, 2008.

Developing a New Optimization Algorithm to Predict the Risk of Car Accidents Due to Drinking Alcoholic Drinks by Using Feed-Forward Artificial Neural Networks

Alaa Saad AHMED[1], Hisham M. KHUDHUR[2]

[1]Computer Science Department, College of Education for Pure Sciences, University of Mosul, Mosul. Iraq
allasaad@uomosul.edu.iq
ORCID: https://orcid.org/0000-0002-4191-1754

[2] Mathematics Department, College of Computer Science and Mathematics, University of Mosul, Mosul, Iraq
hisham892020@uomosul.edu.iq
ORCID: https://orcid.org/0000-0001-7572-9283

Received: 05.08.2021, Accepted: 26.10.2021, Published: 03.01.2022

Abstract — *In this research, we have developed a new algorithm in the field of optimization and its application in teaching artificial neural networks with front feeding to predict the risk of car accidents due to consuming alcoholic beverages, and the algorithm has proven a high efficiency in prediction as it was compared with the results of the model predicting the risk of car accidents due to eating Given alcohol and the results were very close to the true solution to the model.*

Keywords: Artificial Neural Networks, Conjugate Gradient, Machine Learning; Mathematical Modelling,Optimization.
Mathematics Subject Classification: 65K10, 97M10, 90C26.

1 Introduction

In this paper, we try to develop a new algorithm from the traditional (backward) error propagation algorithms by using the pure conjugation condition and applying it in modeling the risk of car accidents due to drinking alcoholic beverages.

It is known that the standard error propagation network represents a successful application of many problems because it is guaranteed to reach the goal if the learning factor is small enough, but it suffers from the problem of slow convergence due to its zigzag path to reach the optimal point resulting from the use of a constant learning factor. During training, in addition to that, there are problems hindering this network, especially in applications of complex problems, and it takes a lot of time to train it, which may take hours as well as thousands of iterations to reach the optimal solution. The performance of this network is

Cite as: *A. S. Ahmed H. M. Khudhur, Developing a new optimization algorithm to predict the risk of car accidents due to drinking alcoholic drinks by using feed-forward artificial neural networks, Journal of Multidisciplinary Modeling and Optimization 4(1) (2021), 11-18.*

affected by many factors, including the choice of the training category, the weights of the primary network, the learning rate, the activation function, the hidden layers and the number of cells in each layer [1] [2].

Our study in this research is focused on a network with a front feeding that consists of the input layer and contains of cells and one hidden layer B of cells and the output layer contains cells as in Figure (1).

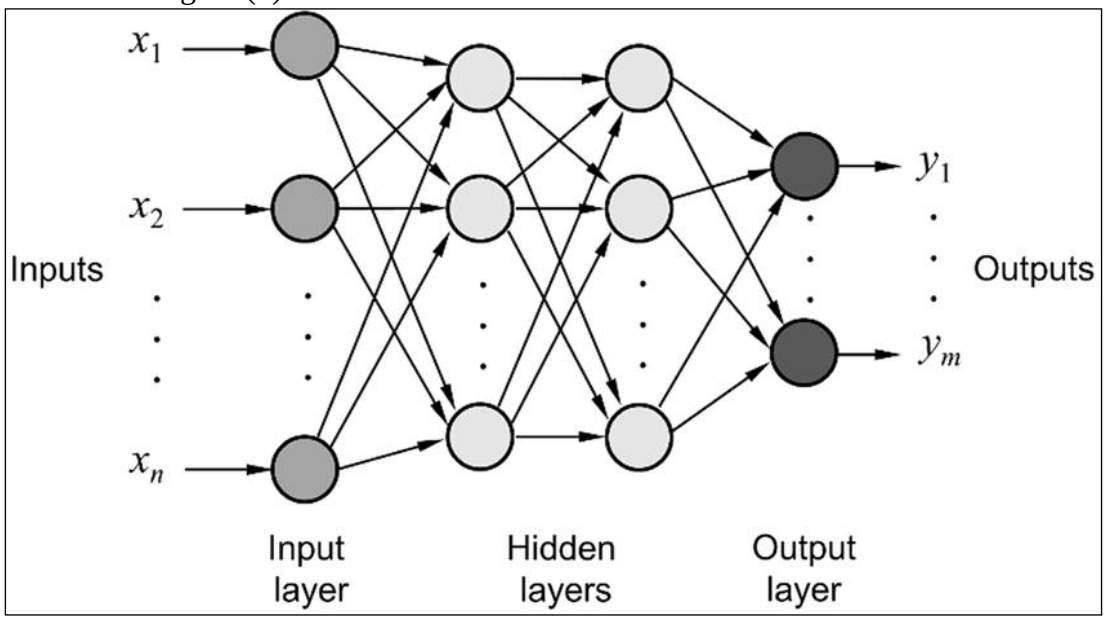

Figure 1. A multi-layered network

Let the training set consist of a pair of target input and output data defined as follows:
$(p_1, t_1), (p_2, t_2), \dots, (p_m, t_m)$

As it $i = 1, 2 \dots, m$ and $t_j \in R^{N_2}$ represents the input vector for each, and represents the target output. And that the network learns through the supervisor (Supervised Training) and in a single batch system (Batch SBP) (Laylani, Abbo, and Khudhur 2018), that is, it provides the network with all the training set $(p_1, t_1), (p_2, t_2), \dots, (p_m, t_m)$ before performing the process of adjusting the weights and after that you adjust the weights as the inclinations calculated in each training example are added to each other to determine the changes in the weights and the wrong function $E(w)$ in this method is as follows :

$$E(w) = \frac{1}{2} \sum_{i-1}^{m} \sum_{j-1}^{m_2} \left(t_{ji} - y_{ji}\right)^2 \tag{1}$$

Since y_{ji} outputs the cell in the output layer depending on the input vector t_{ji}, p_i outputs the desired (target) from the cell j depending on the input vector p_i. We note from equation (1) that teaching the network is achieved if the value of the error function is very small, then it can be said that the issue of teaching a feedforward artificial neural network is to reduce the error function defined in equation (1) according to the one-batch system. (Nguyen and Widrow 1990) The problem can be formulated as follows :

(2)

So N represents the number of weights in the network, and this is an unconstrained optimization problem. Thus, methods and theories of unconstrained examples can be used to solve the above problem.

2 Conjugate Gradient Algorithms

Most of the numerical optimization methods involve two main steps, determining the search direction d_k and calculating the learning factor (step size). In the following, we deal with some methods of numerical optimization. Most optimization algorithms require that the search direction be d_k towards the negative regression of each k, because this characteristic implies that the objective function (error) $E(w)$ will decrease along this direction in general, and the general formula for the search direction in optimization can be written. Not restricted as follows:

$$d_{k+1} = -g_{k+1} + \beta_k d_k \tag{3}$$

If it is $\beta_k = 0$, then the search direction d_k in (3) represents the steepest descent. If the parameter is $\beta \neq 0$, in this case, the method is called conjugate vector (conjugate gradient), and for details see the source [3] [4].

We observed in previous research that the reverse error propagation algorithm uses the derivative of the error function to find the direction of the search,

$$w_{k+1} = w_k + \alpha_k d_k, \;\; k \geq 1$$

Where α_k step-size that satisfy the standard wolfe conditions

$$f(w_k + \alpha_k d_k) \leq f(w_k) + \delta \alpha_k g_k^T d_k$$

$$d_k^T g(w_k + \alpha_k d_k) \geq \sigma d_k^T g_k$$

or strong wolfe conditions

$$f(w_k + \alpha_k d_k) \leq f(w_k) + \delta \alpha_k g_k^T d_k$$

$$|d_k^T g(w_k + \alpha_k d_k)| \leq -\sigma d_k^T g_k$$

$$d_{k+1} = \begin{cases} -g_1, & k = 1 \\ -g_{k+1} + \beta_k d_k, & k \geq 1 \end{cases} \tag{4}$$

The Polak and Ribiere (PRP) [5], Hestenes-Stiefel (HS) [6] and β is scalar.

$\beta_k^{PRP} = \frac{y_k^T g_{k+1}}{g_k^T g_k}$ see [5]

$\beta_k^{HS} = \frac{y_k^T g_{k+1}}{y_k^T d_k}$ see [6]

where $g_k = \nabla f(x_k)$, and let $y_k = g_{k+1} - g_k = \nabla f(x_{k+1}) - \nabla f(x_k)$.

Since $g_{k+1} = E(w)$ is clear that d_k must fulfill the regression property, and for more, see [7] [8] [9] [10] [11] [12] [13] and that weights are updated according to the following relationship:

$$w_{k+1} = w_k + \alpha d_k \tag{5}$$

And now we are developing a new algorithm from the optimization algorithms used in learning feedforward artificial neural networks :

(6)

Now we use the pure conjugation condition by multiplying the above equation by y_k we get

$$\begin{aligned} y_k^T d_{k+1} &= -\theta_k y_k^T g_{k+1} + (1-\theta_k)\beta_k^{PRP} y_k^T d_k = 0 \\ -\theta_k y_k^T g_{k+1} &+ (1-\theta_k)\beta_k^{PRP} y_k^T d_k = 0 \\ -\theta_k y_k^T g_{k+1} &+ (1-\theta_k)\beta_k^{PRP} y_k^T d_k = 0 \\ -\theta_k (y_k^T g_{k+1} &+ \beta_k^{PRP} y_k^T d_k) = -\beta_k^{PRP} y_k^T d_k \\ \theta_k &= \frac{\beta_k^{PRP} y_k^T d_k}{(y_k^T g_{k+1} + \beta_k^{PRP} y_k^T d_k)} = \frac{\beta_k^{PRP}}{\beta_k^{HS} + \beta_k^{PRP}} \end{aligned} \tag{7}$$

We substitute the value of θ_k in (6) to obtain a new research direction and apply it in teaching neural networks

The New Algorithm

Step (1): - Determine the values of each of

1- Primary weights $w_1 \in R^N$.

2- Elementary learning rate parameters $\alpha = 0.01$.

Introductions to stopping metrics

i. $k_{\max}$ The upper limit of repetitions, or so-called (epochs).

ii. goal is the allowable error value.

iii. $T_{\max}$ The upper limit of time.

iv. We calculate $E(w_k), g(w_k)$.

Step (2): - If one of the following measures is achieved. Go to step (7)

1- $E(w_k) < goal$.

2- $k = k_{\max}$.

1- $time \geq T_{\max}$

2- $\|g_k\| < \varepsilon_1$

And vice versa we continue.

Step (3): - calculate the direction of research according to the equation $d_k = -g_k$.

Step (4): - calculate the learning factor α_k .

Step (5): - put $w_{k+1} = w_k + \alpha d_k$.

Step (6): - Put $k = k+1$ then go to step (2).

Step (7): - Pause (Print the results, then stop).

3 Modeling The Risk Of Car Accidents Due To Drinking Alcoholic Beverages [14]

This application deals with modeling the relationship between drinking alcoholic drinks and their application in artificial neural networks.

$$\frac{dR(b)}{d(b)} \propto b \tag{8}$$

By converting this proportion into an equation, the following mathematical model is obtained:

$$\frac{dR(b)}{d(b)} = kb \tag{9}$$

Since k is a constant of proportionality. As is well known the solution of the differential equation

$$R(b) = R(0)e^{kb} \tag{10}$$

So $R(0) = 1$ Because when alcohol is not consumed, there is no risk

$$R(b) = e^{kb}$$

To find the value of the constant k, it is found that when the level of alcohol is in the blood

$$20 = e^{0.14k} \tag{11}$$

If we want to find the percentage of alcohol that leads to a certain risk

(12)

and the results are :

b25=0.1504
b50=0.1828
b75=0.2018
b100=0.2152

Table 1. Percentages of alcohol that lead to certain risk ratios

Alcohol percentage (%)	**0.1504**	**0.1828**	**0.2018**	**0.2152**
Severity (%)	**25**	**50**	**75**	**100**

Therefore, according to this model, when the percentage of alcohol is about 22.0%, the risk ratio is 100% [14].

4 Results of Training Algorithm

In this part of the research we write the results of the learned artificial neural network and a comparison with the results of the exact solution, and as shown in the following table and drawings (4,3 and 5) as drawing (3) illustrates the comparison between the controlled solution and the solution resulting from the artificial neural network education, and the drawing (4) The percentage of risk after teaching the artificial neural networks, and the drawing (5)

shows the square error rate resulting from training the artificial neural network, and the problem was programmed using Matlab 2009 Edition.

Table 2. Results of training algorithm and modeling

Severity (%)	The percentage of alcohol in the human body	The percentage of alcohol after training the network for the algo-rithm
10	**0.1076**	**0.1076**
20	**0.13999**	**0.13999**
30	**0.15893**	**0.15892**
40	**0.17238**	**0.17239**
50	**0.1828**	**0.18281**
60	**0.19132**	**0.19131**
70	**0.19853**	**0.19854**
80	**0.20477**	**0.20476**
90	**0.21027**	**0.21027**
100	**0.21519**	**0.2152**

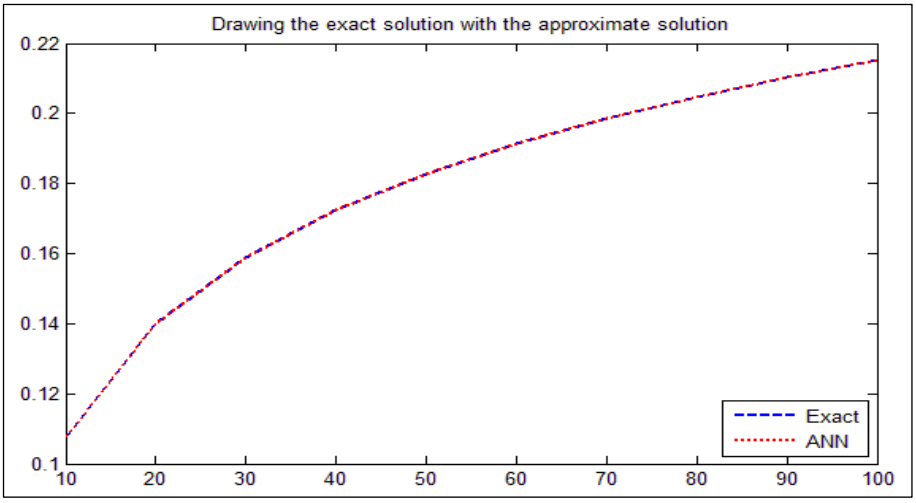

Figure 2. Comparison of Model and Neural Network Approximation

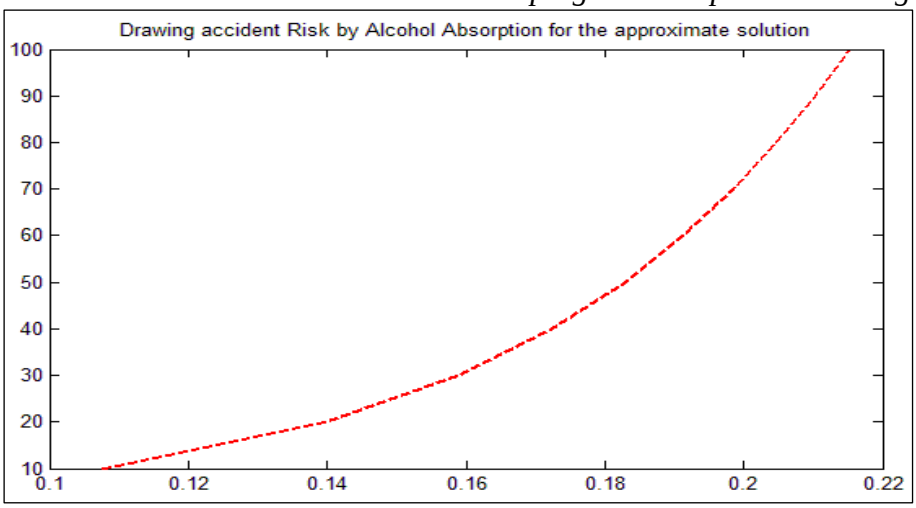

Figure 3. The Risk Ratio after Learning Artificial Neural Networks

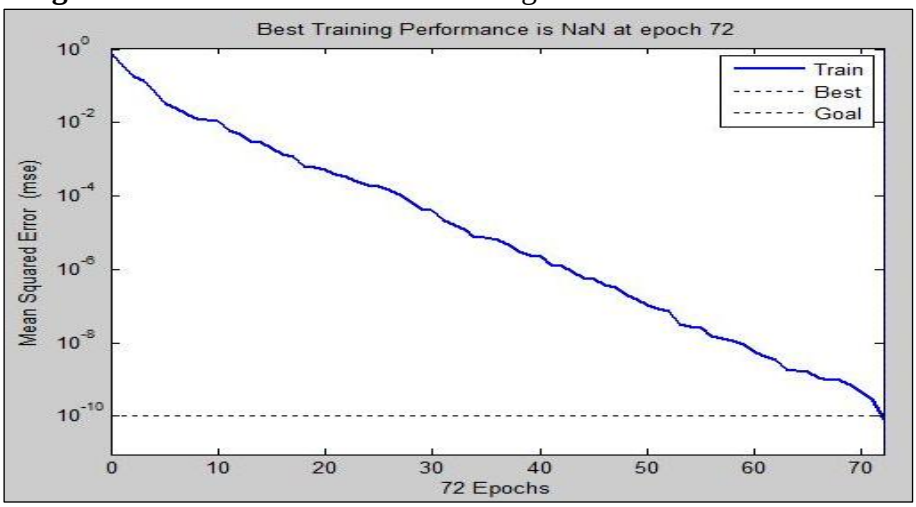

Figure 4. The Square Error Rate for Marking The Network

5 Conclusions

We conclude from the practical results of this research that the artificial neural network with feeding has the ability to predict the risk of car accidents due to alcohol consumption with high accuracy and efficiency, and we also developed the conjugate gradient algorithm to improve the results of the neural network, we can train this neural network to solve other types of problems such as classification problems and regression.

Conflict of Interest Declaration

The authors declare that there is no conflict of interest statement.

Ethics Committee Approval and Informed Consent

The authors declare that there is no ethics committee approval and/or informed consent statement.

References

[1] K. Abbo and M. S Jaborry, Learning rate for the back propagation algorithm based on modified scant equation, Iraqi J. Stat. Sci., 14(26) 2014, 1–11.

[2] Y. A. Laylani, K. K. Abbo, and H. M. Khudhur, Training feed forward neural network with modified Fletcher-Reeves method, Journal of Multidisciplinary Modeling and Optimization, 1(1) 2018, 14–22.

[3] A. Antoniou and W.-S. Lu, Practical Optimization: Algorithms and Engineering Applications. Springer Science & Business Media, 2007.

[4] J. Nocedal and S. Wright, Numerical Optimization. Springer Science & Business Media, 2006.

[5] E. Polak and G. Ribiere, "Note sur la convergence de méthodes de directions conjuguées," ESAIM Math. Model. Numer. Anal. Mathématique Anal. Numérique, 3(R1) 1969, 35-43.

[6] M. R. Hestenes and E. Stiefel, Methods of conjugate gradients for solving linear systems, J. Res. Nat. Bur. Stand.,49 (1) 1952, 409-436.

[7] R. Fletcher and C. M. Reeves, Function minimization by conjugate gradients, Comput. J., 7(2) 1964, 149-154.

[8]Y. H. Dai and Y. Yuan, A nonlinear conjugate gradient method with a strong global convergence property, SIAM J. Optim., 10(1) 1999, 177-182.

[9] L. C. W. Dixon, Conjugate gradient algorithms: quadratic termination without linear searches, IMA J. Appl. Math., 15(1) 1975, 9-18.

[10] K. K. Abbo and H. M. Khudhur, New A hybrid conjugate gradient Fletcher-Reeves and Polak-Ribiere algorithm for unconstrained optimization, Tikrit J. Pure Sci., 21(1) 2015, 124-129.

[11] H. N. Jabbar, K. K. Abbo, and H. M. Khudhur, "Four--term conjugate gradient (CG) method based on pure conjugacy condition for unconstrained optimization," Kirkuk Univ. J. Sci. Stud., 13(2) 2018, 101–113.

[12] K. K. Abbo and H. M. Khudhur, New A hybrid Hestenes-Stiefel and Dai-Yuan conjugate gradient algorithms for unconstrained optimization, Tikrit J. Pure Sci., 21(1) 2015, 118–123.

[13] Z. M. Abdullah, M. Hameed, M. K. Hisham, and M. A. Khaleel, Modified new conjugate gradient method for Unconstrained Optimization, Tikrit J. Pure Sci., 24(5) 2019, 86–90.

[14] B. Y. Al-Khayat, Introduction to Mathematical Modeling Using MATLAB, Dar Ibn Al-Atheer for Printing and Publication University of Mosul, Mosul, 2012.

Journal of Multidisciplinary Modeling and Optimization 4(1) (2021), 19-31.

Identification of Material Using Muography

Muhanad ALYASIRI

[1]Department of Physics, Faculty of Arts and Sciences,
Suleyman Demirel University, Isparta, Turkey
muhanadshamar@gmail.com
ORCID: https://orcid.org/0000-0002-2670-5418

Received: 13.07.2021, Accepted: 27.12.2021, Published: 03.01.2022

Abstract — *Muography is an imaging technique based on the absorption or scattering of atmospheric muons produced from cosmic-ray interactions in the atmosphere. These muons are abundant at sea level and thus provide a natural source for imaging. Scattering density is a characteristic of matter that can be used to discriminate between different materials. When muons pass through material they produce an aggregate of scattering angles with an approximately Gaussian distribution. The standard deviation of the distribution can be calculated using the radiation length of the substance. In this study, we calculated the scattering densities for 20 elements at different four values of the momentum of the muons to show the dependency on the momentum of the incident muons. Our results presented in this study complete the results obtained in some previous related studies.*

Keywords: Cosmic rays, Muography, Material identification.

1 Introduction

Cosmic rays are a natural source of high-energy particles. The study of cosmic radiation remains, even today, fundamental for both subnuclear physics and astrophysics. We know rather well the energy spectrum of cosmic rays. It extends up to $100EeV$ ($10^{20}eV$). At these extreme energies the flux is very low, typically one particle per square kilometer per century. To make a comparison, notice that the highest-energy accelerator, the LHC at CERN, has a center of mass energy of (14 TeV), corresponding to only (0.1 EeV)[1]. Protons or nuclei, which are among the components of cosmic rays, penetrate the atmosphere of the earth and collide with nuclei of the air. This strong interaction produces pion, less frequently kaon mesons and, even more rarely, other hadrons. The produced charged pions have a lifetime of only 26 ns. Thus, the negatively (positively) charged pions quickly decay into muons (anti-muons) and muon anti-neutrions (neutrinos)[2, 3].

Muon is considered from elementary subatomic particle similar to electron but 207 times heavier than electron. Muon was discovered as a constituent of cosmic-ray particle ”showers” in 1936. Because of its mass, it was thought to be particle predicted by

Japanese physicist Yukawa Hideki in 1935 to explain the strong force that binds protons and neutrons together in atomic nuclei[2, 3]. A muon is relatively unstable, with a lifetime of only $2.2\,\mu s$ before it decays by the weak force into an electron and two kinds of neutrinos. Since muons are charged particles, before decaying, they lose energy by displacing electrons from atoms through ionization process. At velocities close to the speed of light, ionization dissipates energy in relatively small amounts, so muons in cosmic radiation are extremely penetrating and thus can travel to some distances below earth surface.The interest in the use of muons for imaging issues in the field of Earth Sciences, as said before, emerged soon after the discovery of these particles and their properties. Muons found in cosmic rays can go through hundreds of meters (the most energetics also through kilometers) of rock, undergoing attenuations related to the quantity of matter traversed [4]. Initially, the muons imaging technique was born from the need to characterize from a geological point of view the structures in the underground labs that hosted particle detectors. Subsequently, when the devices used to carry out these measurements became more portables, also measurements of geological structures such as mines, mountains, and volcanoes were conducted, with the aim of monitoring natural phenomena such as earthquakes or eruptions. The first idea to exploit the muon physical characteristics was, therefore, to use the information on the absorption of muons to measure the thickness of the material traversed by cosmic rays. The first application of cosmic rays to inspect large volumes was performed in 1955 when the thickness of a layer of rock overlying an underground tunnel was measured by E.P. George [5]. An application much more spectacular was conceived by the Nobel Prize in physics LW Alvarez [6] in 1970, in which he made radiography of the pyramid of Khafre, in order to look for hidden chambers. Recently, the same technique was used to inspect the interior of volcanoes. The operating principle is the same as the X-ray radiography. The measured quantity is the flux attenuation of the muon that crosses the target under the study. Based on this, the quantity of material encountered by muons along their trajectory can be estimated. The interaction of the muons flux with the target depends on both the size of the target and its density: thus for a small size and a low density only a few muons will interact, while a body of a large size or s dense body, most of the striking muons will be absorbed.

Though there are previous studies on the interaction of muon with materials, applications have emerged in various fields. Driven by the deep penetrating power of muons and the non-destructive feature of muography as an imaging technique, many proposals exist for using this technique in several fields. Among these fields, one can mention volcanology, archeology, security, nuclear reactor and waste imaging, underground measurements, civil engineering and material identification.

2 PRINCIPLES OF MUOGRAPHY TECHNIQUE

Muon reaction with matter in range (1-1000 GeV) , where be two interaction ways : Energy loss through electromagnetic interaction with electrons causing ionization, and deflection via Coulomb's multiple scattering. The distribution of scattering angles is well approximated by the Gaussian distribution[9]:

$$f_{\theta_x}(\theta_x) = \frac{1}{\sqrt{2\pi}\sigma_\theta} \exp(-\frac{\theta_x^2}{2\sigma_\theta^2}) \tag{1}$$

Where σ_θ is the Root Mean Square (RMS) width of the angular distribution. Therefore one can determine the density and the atomic number of the object of interest by the measurement of the scattering angles of the particles which penetrate the object and given by the following equation[7]:

$$\sigma_\theta = \frac{13.6}{p\beta c} z \sqrt{\frac{L}{L_{rad}}} [1 + 0.038 \ln(\frac{L}{L_{rad}})] \tag{2}$$

Where p is the momentum, and ($\beta c = 1$ for muons) is the velocity of the incident particle, L is the depth of the material, z atomic number and L_{rad} is the radiation length of the material. Represent radiation length of material is mean length to reduce from the energy of an electron by factor 1/e. which will be affected the electron when arriving in the vicinity of an atom, where electrons will emit photons' which will reduce energy depend on the number of electrons of the atom and also on the size of the atom, represented by its atomic weight A[8].

$$L_{rad} = \frac{716.4}{Z(Z+1)\ln\frac{287}{\sqrt{Z}}}\ g.cm^{-3} \tag{3}$$

If we have a composite material with number of different materials, we can also estimate the combined radiation length of the sample.The general formula for the radiation length is then given as[8]:

$$\frac{W_o}{L_o} = \sum \frac{W_i}{L_i} \tag{4}$$

where W_o is the total mass of the sample in g,L_o is the combined radiation length of the sample in gcm^2,W_i is the mass of the individual component in g and L_i is the radiation length of the individual component in gcm^2.

The aim of multiple scattering theory is to predict σ_θ given with scattering material, thickness, and incident particle energy. In this theory, Moliere derived an accurate formula for single scattering in the screened Coulomb field of nucleus and also through using that formula he computed multiple scattering.

Moliere's approach to describe multiple scattering of fast charged particles is based on his theory of the single scattering process (each scattering of a particle off one atom is regarded as an independent on other scattering). It is shown that the scattering depends only on the atomic screening; the critical angle χ_a [12]. Assuming that all scattering angles are small i.e. $sin\theta \simeq \theta$ and the scattering problem is equivalent to diffusion in the plane of θ, the number of charged particles in the angular interval $d\theta$ after passing a thickness t is $f(\theta, t)\theta d\theta$. Here, $f(\theta, t)$ can be calculated as [7, 8, 11]:

$$f(\theta, t) = \int_0^\infty \eta d\eta J_o(\eta\theta) \times \exp[-Nt \int_0^\infty \sigma(x) x dx \{1 - J_o(\eta x)\}] \tag{5}$$

Where N is the number of scattering atoms per cm^3,t is thickness material, θ is the scattering angle, $\sigma(x)\, x\, dx$ is the differential scattering cross section into the angular interval dx and J_o Bessel transformation. The scattering from atoms is characterized by the fact that σ decreases and it is complicated only for angles of the order of:

$$\chi_o = \frac{\bar{\lambda}}{a} = \frac{\bar{\lambda}}{(0.885 a_o Z^{-\frac{1}{2}})} \tag{6}$$

Where $\bar{\lambda}$ is the de Broglie wavelength of the electron, a_o the Bohr radius, and a the Fermi radius of the atom. For any reasonable foil thickness, the width of the multiple scattering distribution is very large compared with χ_o.

$$Nt\sigma(x)xdx = 2\chi_c^2 xdxq(x)/x^4 \tag{7}$$

Here

$$\chi_c^2 = 4\pi Nte^4 Z(Z+1)z^2/(\rho\upsilon)^2 \quad rad^2(electrons) \tag{8}$$

$$\chi_c^2 = 4\pi Nte^4 Z^2 z^2/(\rho\upsilon)^2 \quad rad^2(heavy\, particles) \tag{9}$$

Where p is the momentum and υ represents the velocity of the scattered particle of charge z. The factor $Z+1$ instead of Z is to take into account the scattering by the electrons of atoms. The physical meaning of χ_c is that the total probability of single scattering through an angle greater than χ_c, is exactly one.
As first suggested, in Ref. [10], Moliere's transformed equation, takes simpler form compared to equation (5) as:

$$f(\theta)\theta d\theta = \lambda d\lambda \int_0^\infty y dy J_o(\lambda y) \exp[\frac{1}{4}y^2(-b + \ln\frac{1}{4}y^2] \tag{10}$$

$$b = \ln(\chi_c/\chi_a)^2 + 1 - 2C \equiv \ln(\chi_c/\chi_a)^2 \tag{11}$$

Where $C = 0.577$ is Euler's constant, $\lambda = \theta/\chi_c$, $y = \chi_c\eta$. The important result of Moliere's theory is that the scattering is described by a single parameter; the screening angle (χ_a). As can be seen from Eq.(10), the distribution function $f(\theta)$ depends on b and from Eq.(11) b depends on the ratio of the unit probability angle (χ_c), in equation(9), that describes the foil thickness to the screening angle (χ_a) which describes the scattering atom. The distribution function $f(\theta)$ is entirely independent of the shape of the differential cross section [11].
For the actual determination of the screening angle χ_a Moliere uses his own calculation of the single scattering by a Thomas-Fermi potential which does not make use of the Born approximation, the solution being accomplished by means of the Wentzel Kramers Brillouin (WKB) method, which is a method for finding approximate solutions to linear differential equations with spatially varying coefficients. It is typically used for a semiclassical calculation in quantum mechanics in which the wave function is recast as an exponential function, semiclassically expanded, and then either the amplitude or the phase is taken to be changing slow[11].

$$\chi_a = \chi_o\sqrt{(1.13 + 3.76\alpha^2)} \tag{12}$$

With α being the usual parameter the Born approximation, [11],

$$\alpha = zZe^2/\hbar\vartheta \tag{13}$$

For the actual determination of the screening angle (χ_a)Moliere uses his own calculation" of the single scattering by a Thomas-Fermi potential which does not make use of the Born approximation.

$$\alpha = \frac{zZ}{(137\beta)} \approx \frac{1}{137} \tag{14}$$

3 RESULTS

In this section we present our results. We consider a target material of thickness (10 cm) in accordance with a previous study carried in 2001 where out by Christopher Morris and William Priedhorsky of Los Alamos National Laboratory (LANL) and considered as a novel form of radiography. Their idea was to make use of the multiple Coulomb scattering experienced by cosmic ray muons passing through objects to segregate materials of high and low atomic density. Morris and Priedhorsky set together a small team of researchers at LANL, including themselves. The goal of this team was to provide a proof of the principle for cosmic-ray muon radiography. To achieve this goal the team outlined four primary objectives. These objectives are building a small prototype and gather experimental data, implementing a Monte Carlo simulation of the experiment, developing an object reconstruction algorithm and producing reconstructions of experimental data (to prove the concept) and simulated data (to validate understanding)). By 2003 these objectives were achieved and documented in Ref.[16]. A new form of radiography of small objects, based on using passive cosmic ray muons, was introduced. A significant amount of press attention followed, and cosmic ray muon radiography was featured in Physics Today [17], on National Public Radio [18], and several websites, including those of National Geographic [19], Science News [20], and the BBC.

The technique exploits the multiple Coulomb scattering of muons for non-destructive inspection without the use of artificial radiation. The muon sources used in the technique were originating from cosmic rays with the typical sea-level flux. The energy of the muons were ranging between 1 GeV-10 GeV with average 3 GeV-4 GeV.

The scattering density is a characteristic of the material. It depends on the standard deviation of the distribution of scattering angles produced as a result of the scattering of muons after exiting material. We will evaluate the standard deviation using two different methods; using the radiation length L_{rad} and using a simple Gaussian approximation of Moliere's theory which will be discussed in the following.

3.1 Materials Identification Based On Radiation Length

When charged particles cross a matter they produce aggregate of scattering angles θ and displacements from the un-scattered exit point. The angular scattering distribution is approximately Gaussian. The standard deviation of both distributions may approximately be expressed in terms of material properties as[9]

$$\sigma_\theta \cong \frac{15}{p_\circ}\sqrt{\frac{L}{L_{rad}}} \tag{15}$$

It is clear from the equation that a large depth of a lower Z (higher L_{rad}) material may produce a scattering equivalent to that produced by a higher Z (lower L_{rad}) material. Scattering is also influenced by particle momentum p. To identify material it is necessary to normalize for these two effects[12, 14]. Establishing a nominal muon momentum p_o and squaring both sides of equation (15):

$$\sigma_\theta^2 = (\frac{15}{p_o})^2[\frac{1}{L_{rad}}]L \tag{16}$$

The scattering density of a material with radiation length L_{rad} is defined as:

$$\lambda \equiv (\frac{15}{p_o})^2\frac{1}{L_{rad}} \tag{17}$$

And thus from equation(16) we have

$$\lambda = \frac{\sigma_\theta^2}{L} \tag{18}$$

Scattering density therefore expresses the mean square of the scattering distributions expected for muons with nominal momentum passing through a unit depth of a material with radiation length L_{rad}. In Tables(1,2,3,4) we list the values of the radiation lengths of three different classes of elements used in this study. In the following, we present our results of the scattering densities for 20 different elements at different values of momenta of the muons(1,3,4 and 10 GeV). The results for low-Z materials are presented in Fig.1. For medium-Z materials our results are presented in Fig 2 and finally for the case of high-Z materials our results are plotted in Fig.3.

3.1.1 Scattering density of three different classes of elements at momentum 1GeV

In Table(1), we present our results for evaluation of the standard deviation σ and scattering density λ of three different classes of elements based on their atomic number Z at momentum equal ($1GeV$) using radiation length as an input parameter. Note that the scattering density is very small for gases compared to other materials.The large values of scattering densities in solids is due to the small distance between the nuclei of their atoms, which causes an increase in attraction and repulsion between the muons and nuclei of the atoms.

Table 1: Scattering densities of three different classes of elements at momentum equal $1GeV$.,where G:Gas,L:Liquid and S:Solid.

1-Low-Z Material						
Z	Material	Symbol	State	$L_{rad}(cm)$	$\sigma(mrad^2)$	$\lambda(mrad^2/cm)$
1	Hydrogen	H	G	752300	0.0546885	0.000299083
2	Helium	He	G	560000	0.0633866	0.000401786
3	Lithium	Li	S	155	3.81	1.45161
4	Beryllium	Be	S	35.3	7.98369	6.37394
6	Carbon	C	S	18.8	10.9399	11.9681
7	Nitrogen	N	G	33100	0.260722	0.00679758
8	Oxygen	O	G	25800	0.295312	0.00872093
10	Neon	Ne	G	24.0	9.68246	9.375
13	Aluminum	Al	S	8.9	15.9	25.2809
14	Silicon	Si	S	9.36	15.5043	24.0385
18	Argon	Ar	G	14.0	12.6773	16.0714
2-Medium-Z Material						
26	Iron	Fe	S	1.76	35.7548	127.841
29	Copper	Cu	S	1.43	39.6664	157.343
35	Bromine	Br	L	3.71	24.6266	60.6469
47	Silver	Ag	S	0.86	51.1496	261.628
53	Iodine	I	S	1.74	35.9597	129.31
3-High-Z Material						
74	Tungsten	W	S	0.35	80.1784	642.857
79	Gold	Au	S	0.3344	82.0272	672.847
82	Lead	Pb	S	0.56	63.3866	401.786
92	Uranium	U	S	0.3166	84.3016	710.676

3.1.2 Scattering density of three different classes of elements at momentum 3GeV

In Table(2), we present our results for evaluation of the standard deviation σ and scattering densities λ at momentum equal ($3GeV$). We observe similar results to the previous case. It is possible to distinguish between different materials through the different ranges of the scattering densities where (low-Z materials have $\lambda \leq 5$, medium-Z materials have $5 < \lambda \leq 30$ and high-Z materials have $\lambda \geq 30$)[9].

Table 2: Scattering densities of three different classes of elements at momentum equal $3GeV$.

1-Low-Z Material						
Z	Material	Symbol	State	$L_{rad}(cm)$	$\sigma(mrad^2)$	$\lambda(mrad^2/cm)$
1	Hydrogen	H	G	752300	0.0182295	0.0000332314
2	Helium	He	G	560000	0.0211289	0.0000446429
3	Lithium	Li	S	155	1.27	0.16129
4	Beryllium	Be	S	35.3	2.66123	0.708215
6	Carbon	C	S	18.8	3.64662	1.32979
7	Nitrogen	N	G	33100	0.0869072	0.000755287
8	Oxygen	O	G	25800	0.0984374	0.000968992
10	Neon	Ne	G	24.0	3.22749	1.04167
13	Aluminum	Al	S	8.9	5.29999	2.80899
14	Silicon	Si	S	9.36	5.16811	2.67094
18	Argon	Ar	G	14.0	4.22577	1.78571
2-Medium-Z Material						
26	Iron	Fe	S	1.76	11.9183	14.2045
29	Copper	Cu	S	1.43	13.2221	17.4825
35	Bromine	Br	L	3.71	8.20886	6.73854
47	Silver	Ag	S	0.86	17.0499	29.0698
53	Iodine	I	S	1.74	11.9866	14.3678
3-High-Z Material						
74	Tungsten	W	S	0.35	26.7261	71.4286
79	Gold	Au	S	0.3344	27.3424	74.7608
82	Lead	Pb	S	0.56	21.1289	44.6429
92	Uranium	U	S	0.3166	28.1005	78.964

3.1.3 Scattering density of three different classes of elements at momentum 4GeV

In Table(3), we present our results for evaluation of the standard deviation σ and scattering density λ at momentum equal ($4GeV$).

3.1.4 Scattering density of three different classes of elements at momentum 10GeV

In Table(4), we present our results for evaluation of the standard deviation and scattering densities at momentum equal ($10GeV$). Note that scattering densities of gas state materials are very small compared to other materials. This can be explained as the nuclei of atoms of gaseous materials have a small effect on the muons passing between them due to the large distances between these atoms, compared with solid and liquid materials. The decrease in the scattering densities in materials can be explained as the increasing of muons momenta leads to a decrease in attraction and repulsion between the muons and nuclei of the atoms.

In Figures (1, 2, 3), we show our results of scattering densities of low-Z,medium-Z, and high-Z materials at different momenta. We note from the figures that, at the momenta of muon 1 GeV and 3 GeV gases with small atomic numbers do not appear as they have small

Table 3: Scattering densities of three different classes of elements at momentum equal $4GeV$.

1-Low-Z Material						
Z	Material	Symbol	State	$L_{rad}(cm)$	$\sigma(mrad^2)$	$\lambda(mrad^2/cm)$
1	Hydrogen	H	G	752300	0.0136721	0.0000186927
2	Helium	He	G	560000	0.0158466	0.0000251116
3	Lithium	Li	S	155	0.952501	0.0907258
4	Beryllium	Be	S	35.3	1.99592	0.398371
6	Carbon	C	S	18.8	2.73497	0.748005
7	Nitrogen	N	G	33100	0.0651804	0.000424849
8	Oxygen	O	G	25800	0.0738281	0.000545058
10	Neon	Ne	G	24.0	2.42061	0.585938
13	Aluminum	Al	S	8.9	3.97499	1.58006
14	Silicon	Si	S	9.36	3.87609	1.5024
18	Argon	Ar	G	14.0	3.16933	1.00446
2-Medium-Z Material						
26	Iron	Fe	S	1.76	8.93871	7.99006
29	Copper	Cu	S	1.43	9.91661	9.83392
35	Bromine	Br	L	3.71	6.15665	3.79043
47	Silver	Ag	S	0.86	12.7874	16.3517
53	Iodine	I	S	1.74	8.98994	8.0819
3-High-Z Material						
74	Tungsten	W	S	0.35	20.0446	40.1786
79	Gold	Au	S	0.3344	20.5068	42.0529
82	Lead	Pb	S	0.56	15.8466	25.1116
92	Uranium	U	S	0.3166	21.0754	44.4172

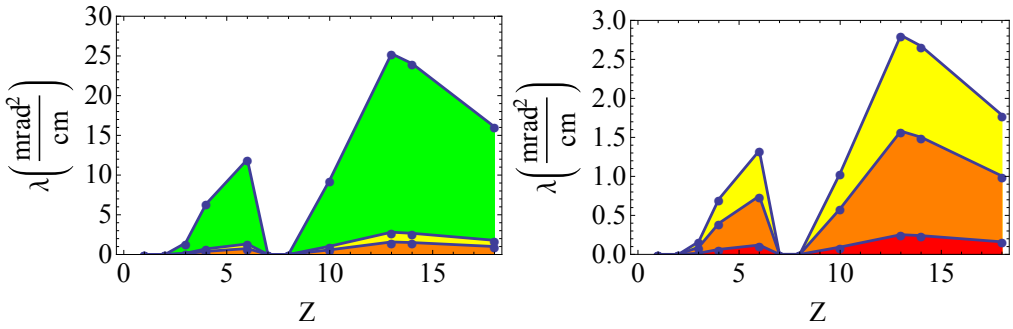

Figure 1: Scattering densities of low-Z materials. In the left, green, yellow and orange colors correspond to muon momenta 1, 3 and 4 GeV respectively. In the right, yellow, orange and red colors correspond to muon momenta 3, 4 and 10 GeV respectively.

values of the scattering densities, while other materials can be distinguished according to their scattering densities. We also note that the scattering density of tungsten is greater than that of lead although lead has a larger atomic number than that of tungsten. This is because the density of tungsten is larger than the density of lead. At the momentum of

Table 4: Scattering densities of three different classes of elements at momentum equal $10GeV$.

1-Low-Z Material						
Z	Material	Symbol	State	$L_{rad}(cm)$	$\sigma(mrad^2)$	$\lambda(mrad^2/cm)$
1	Hydrogen	H	G	752300	0.00546885	0.00002990830
2	Helium	He	G	560000	0.00633866	0.00004017860
3	Lithium	Li	S	155	0.381	0.0145161
4	Beryllium	Be	S	35.3	0.798369	0.0637394
6	Carbon	C	S	18.8	1.09399	0.119681
7	Nitrogen	N	G	33100	0.0260722	0.0000679758
8	Oxygen	O	G	25800	0.0295312	0.0000872093
10	Neon	Ne	G	24.0	0.968246	0.09375
13	Aluminum	Al	S	8.9	1.59	0.252809
14	Silicon	Si	S	9.36	1.55043	0.240385
18	Argon	Ar	G	14.0	1.26773	0.160714
2-Medium-Z Material						
26	Iron	Fe	S	1.76	3.57548	1.27841
29	Copper	Cu	S	1.43	3.96664	1.57343
35	Bromine	Br	L	3.71	2.46266	0.606469
47	Silver	Ag	S	0.86	5.11496	2.61628
53	Iodine	I	S	1.74	3.59597	1.2931
3-High-Z Material						
74	Tungsten	W	S	0.35	8.01784	6.42857
79	Gold	Au	S	0.3344	8.2027	6.72847
82	Lead	Pb	S	0.56	6.3386	4.01786
92	Uranium	U	S	0.3166	8.43016	7.10676

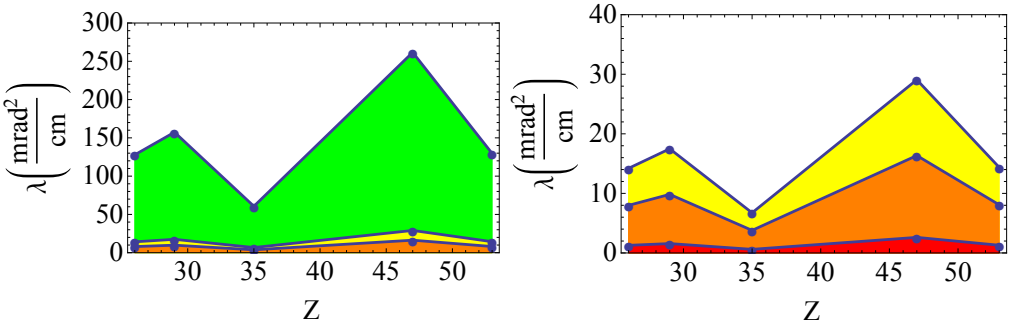

Figure 2: Scattering densities of medium-Z materials. In the left, green, yellow and orange colors correspond to muon momenta 1, 3 and 4 GeV respectively. In the right, yellow, orange and red colors correspond to muon momenta 3, 4 and 10 GeV respectively.

muon 4 GeV, we observe the same results but the only difference is that, the scattering density value of each material decrease with increasing the momentum of the muons. At the momentum of muon 10 GeV, we notice from the figures that there is a decrease in

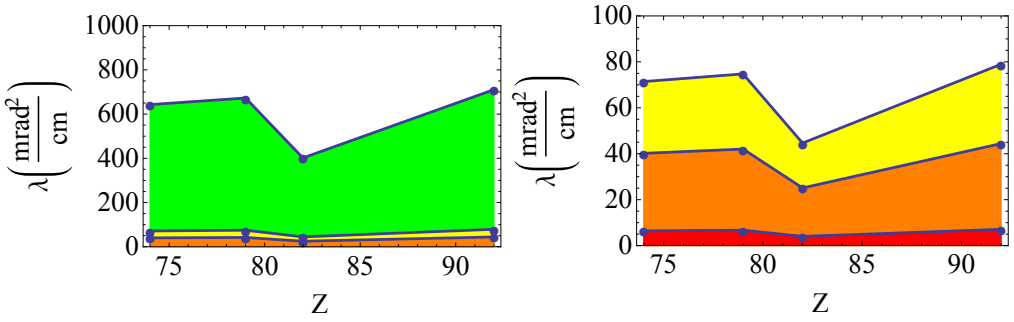

Figure 3: Scattering densities of high-Z materials. In the left, green, yellow and orange colors correspond to muon momenta 1, 3 and 4 GeV respectively. In the right, yellow, orange and red colors correspond to muon momenta 3, 4 and 10 GeV respectively.

the scattering density value of each material with increasing the momentum of the muons as in the previous cases. Note that scattering densities of gaseous state materials are very small compared to other materials. This can be explained as the nuclei of atoms of gaseous materials have a small effect on the muons passing between them due to the large distances between these atoms, compared with solid and liquid materials. In all figures, the decrease in the scattering densities with increasing muon momenta, for all materials, can be explained as increasing the muons momenta leads to a decrease in attraction and repulsion between the muons and nuclei of the atoms.

Finally the results of this study is based on Moliere's interpretations of the charged particles with matter [10, 11] and the study done in the laboratory of Los Alamos National Laboratory (LANL) in which only three different materials (iron - concrete - uranium) were studied at the muon energies(3 - 4) GeV [7, 9]. It should be note that in this study we consider 20 different materials for the range of muon energies (1 - 3 - 4 - 10) GeV.

4 CONCLUSIONS

Muography as an imaging technique is based on the absorption or scattering of atmospheric muons produced from cosmic-ray interactions in the atmosphere. This technique has the ability to investigate the interior of natural or artificial structures and can help, for instances, to make a surveys on nuclear wastes, homeland security, monitoring of natural hazard such as volcanic eruptions and material identifications. When muons pass through material they produce aggregate of scattering angles with an approximate Gaussian distribution. Theoretically, the standard deviation of the distribution can be calculated using the radiation length of the substance. Since scattering density depends on the standard deviation of the distribution, we therefore have provided our results for the scattering densities of 20 elements ranging from low, medium and high Z number. For these 20 elements, we calculated their scattering densities at different four values of the momentum of the muons, namely at momenta (1, 3, 4 and 10 GeV) to show its dependency on the momentum. This technique has the ability to break through the big thickness of materials in the comparison with another technique as example x-ray, without causing any damage to the inspected materials. As demonstrated in previous studies, where it has been shown to be effective in detecting substances, references can be reviewed at [2, 7, 21, 22]

Conflict of Interest Declaration

The authors declare that there is no conflict of interest statement.

Ethics Committee Approval and Informed Consent

The authors declare that there is no ethics committee approval and/or informed consent statement.

References

[1] A. Bettini, Introduction to Elementary Particle Physics, Cambridge University Press, Cambridge, 2008.

[2] S. Procureur, Muon imaging Principles, technologies and applications, Nucl. Instrum. Methods Phys. Res A., 878 2018, 169-179.

[3] P. K. F. Grieder, Cosmic Ray at Earth Researcher's Reference and Data Book, Elsevier, Amsterdam, 2001.

[4] K. Nagamine. Introductory Muon Science. Cambridge University Press, Cambridge, 2003.

[5] E.P. George. Cosmic rays to inspect large volumes. Commonwealth Engineer, 1955, 455-457.

[6] L. W. Alvarez, J.A. Anderson, F.E. Bedwei, J. Burkhard, A. Fakhry, A. Girgis, A. Goneid, F. Hassan, D. Iverson, G. Lynch, et al. Search for hidden chambers in the pyramids. Science New York, 167(3919) 1970, 832.

[7] Marilena Bandieramonte, Muon Portal project: Tracks reconstruction, automated object recognition and visualization techniques for muon tomography data analysis, IEEE International Conference on Technologies for Homeland Security, 2015, 517-522.

[8] M. Gupta, Calculation of radiation length in materials,PH-EP-Tech-Note, 2010-013.

[9] L. J. Schultz, K.N.Borozdin, J.J. Gomez, G.E.Hogan, J.A. McGill, C.L. Morris, W. C. Priedhorsky, A. Saunders, M.E.Teasdale, Image reconstruction and material Z discrimination via cosmic ray muon radiography, Nucl. Instrum. Methods Phys. Res A, 519 2004, 687-694.

[10] Scott. WT, the theory of small-angle multiple scattering of fast charged particles, Reviews of modern physics,1963, volume 35 pages231.

[11] H. A. Bethe, Moliere's theory of multiple scattering, Phys. Rev., 89 1953, 1256.

[12] P. La Rocca, V. Antonuccio, M. Bandieramonte, U. Becciani, F. Belluomo, M. Belluso, S. Billotta, A. A. Blancato, D. Bonanno, G. Bonanno, Search for hidden high-Z materials inside containers with the Muon Portal Project,J. Instrum., 9 2014, C01056.

[13] L. Cremonesi, Cosmic ray muon tomography for anti-terrorism applications, Master Thesis, University College of London, 2011.

[14] G. R. Lynch and O. I. Dahl, Approximations to multiple coulumb scattering, Nucl. Instrum. Methods Phys. Res B, 58 1991, 6-10.

[15] S. I. Dutta, M. H. Reno, I. Sarcevic, and D. Seckel, Propagation of muons and taus at high energies, Phys. Rev. D, 63 2001, 094020.

[16] K. N. Borozdin, G. E. Hogan, C. M., W. C. Priedhorsky, A. Saunders, L. J. Schultz, M. E. Teasdale, Radiographic Imaging with Cosmic Ray Muons, Nature 422 2003, 277.

[17] B. Schwarzschild, Cosmic-ray muons might help thwart transport of concealed fissile material, Physics Today, 56(5) 2003, 19-22.

[18] National Public Radio,Detecting Nuclear Smugglers, All Things Considered radio broadcast,June 13, 2003.

[19] J. Roach, Cosmic Particles could Detect Nuke Materials, National Geographic News, 2003.

[20] P. Weiss, Muon Manna? Particle Shower may Spotlight Loose Nukes, Science News Online, 163 2003, 179.

[21] L. Olah, Research and development of particle detectors for muon tomography and the CERN ALICE experiment, PhD Thesis, Budapest, 2016.

[22] N. Lesparre, D. Gilbert, Y. Marteau, Y. Declais, D. Carbone and E. Galicet, Geophysical muon imaging: feasibility and limits, Geophys. J. Int. 183(3), (2010), 1348-1361.